
Investigation of the Ultrasonic Backscattering in Modelled Surface Hardened Samples using Finite Element Method.

By Charles Ford

Supervised by Dr. Jie Zhang



Department of Mechanical Engineering
University of Bristol
2024

Abstract

Surface hardening is a common manufacturing technique with applications across various industries. Presently, assessing case depth in this process requires destructive methods, emphasising the need for advancements in non-destructive evaluation. This study presents an investigation into the ultrasonic backscattering in surface hardened samples using finite element analysis. Voronoi tessellations were utilised to construct polycrystalline grains and Euler angles were used to assign random orientation, resulting in a statistically isotropic material. Two models with different grain morphologies and uniformity were investigated. Each model consists of a 6x1.5mm sample divided into sections G1 and G2, with an average grain size of 15 μm and 30 μm respectively. 20 realisations for each model were executed to capture varied microstructure configurations. The spatial variance of the realisations is determined and then processed using the Rayleigh maximum likelihood estimation (RMLE) method. Results demonstrate a correlation between grain morphology and backscatter response. The RMLE method proved successful in predicting the boundary between G1 and G2, achieving a precision within 1% of actual position. Various avenues for further work were discussed, including conducting an experimental comparison and utilising different input parameters. In summary, this study provides insight on the potential of ultrasonic backscattering and the RMLE method in non-destructive evaluation applications.

Declaration

This project report is submitted towards an application for a degree in Mechanical Engineering at the University of Bristol. The report is based upon independent work by the candidate. All contributions from others have been acknowledged and the supervisor is identified on the front page. The views expressed within the report are those of the author and not of the University of Bristol.

I hereby assert my right to be identified as the author of this report. I give permission to the University of Bristol Library to add this report to its stock and to make it available for consultation in the library, and for inter-library lending for use in another library. It may be copied in full or in part for any bona fide library or research worker on the understanding that users are made aware of their obligations under copyright legislation.

I hereby declare that the above statements are true.

A handwritten signature in black ink, appearing to be 'CF' with a stylized flourish.

© Charles Ford, 2024

Certification of ownership of the copyright in a dissertation presented as part of and in accordance with the requirements for a degree in Mechanical Engineering at the University of Bristol.

This report is the property of the University of Bristol Library and may only be used with due regard to the author. Bibliographical references may be noted but no part may be copied for use or quotation in any published work without prior permission of the author. In addition, due acknowledgement for any use must be made.

Acknowledgements

I would like to extend my gratitude to Dr. Jie Zhang and Zixin Guo for their invaluable insights on NDE processes and for their support throughout this project.

Contents

1	Introduction	4
1.1	Aims and Objectives	5
2	Methodology	6
2.1	Microstructure Generation	6
2.1.1	Generating Grain Positions	7
2.1.2	Assigning random orientation to grains	7
2.2	Finite Element Model	9
2.2.1	Experimental Set-Up	9
2.2.2	Mesh Convergence	10
2.3	Signal Processing	12
2.3.1	Rayleigh Maximum Likelihood Estimate	12
2.3.2	Spatial Variance	13
3	Results & Discussion	14
3.1	Two-point Correlation Function & Probability Density Function	14
3.2	Signal Processing Results	16
4	Conclusion	17
4.1	Further Work	18
	References	19

1 Introduction

Surface hardening techniques represent a widely adopted approach that enhance the mechanical properties of steel components, including surface hardness, fatigue endurance, and resistance to wear [1, 2]. Hardening methods such as induction heating [3, 4] realise these improvements through rapid heating, resulting in a case depth of finer martensite grains on the surface of the steel. The refined grains prevent cleavage crack propagation leading to improved toughness of the component [5].

Currently, evaluating the case depth of steels involves destructive, costly, and time-consuming procedures [6]. Consequently, there is a growing interest in utilising non-destructive evaluation (NDE) methods to measure case depth in such materials [7]. Ultrasonic techniques are a common approach in NDE and have been demonstrated to effectively assess the depth of hardened steel. For instance, Hornarvar et al. [8] employed a deconvolution method termed Wiener filtering, which enhanced the resolution of ultrasound echoes from the surface to the transition zone between the hardened layer and the soft core of their sample. Later, they applied an ultrasonic backscattering technique, incorporating the Savitzky-Golay smoothing filter and a moving average method which smoothed signals while preserving original amplitude values [9]. These investigations utilise the scattering phenomena evident in the material microstructure, distinguishing between fine martensite grains in the case depth and a coarser pearlite-ferrite structure in the transition zone. Therefore, comprehending the propagation of ultrasonic waves and understanding why this occurs within microstructures is essential. [10].

Ultrasonic measurements have been extensively employed in understanding the characteristics of microstructures. Mason and McSkimmin [11] pioneered investigations in this field, identifying that the primary cause of ultrasonic scattering and attenuation within polycrystalline materials is the acoustic impedance mismatch at grain boundaries, a phenomenon termed Rayleigh scattering. Kino and Stank [12] later built upon this understanding, developing a unified theory that relates ultrasonic attenuation to both microscopic and macroscopic properties of materials, applicable to locally inhomogeneous and anisotropic materials. The unified theory confirms that when ultrasonic waves propagate through polycrystalline materials, they scatter at grain boundaries due to grain anisotropy and misorientation [13]. This scattering phenomena provides information on a material's microstructure non-destructively, and has therefore found application in various NDE studies, including crack and defect detection [14, 15], characterising backscattering behaviour [16, 17], examination of grain properties such as size [18], shape and texture [19], as well as characterisation of case depth [8, 9].

In the study for characterising the ultrasonic backscatter in a microstructure, Goshal and Turner [16, 17] developed a time-dependent spatial variance model of ultrasonic backscatter with respect to an assumption of a singly-scattered response (SSR) to microstructural properties. Microstructure information was determined from the amplitude of the spatial variance curve, which was calculated over a number of positions along their steel and aluminium samples. This method was later utilised by Du et al. [20] in order to analyse the backscattering difference in unquenched and quenched steels used in a railroad wheel, where it was found that the spatial variance amplitude drops dramatically near the tread surface, indicating a change in the backscattering signal due to the fine lamellar spacing of the pearlite created due to quenching. This method exhibits high sensitivity to microstructure changes, which may prove useful in applications with a number of backscattering measurements.

More recently, finite element (FE) techniques have been employed to interpret the backscattering in polycrystalline materials further, demonstrating its considerable potential in advancing the field of NDE for such materials [21–23]. Unlike other existing theoretical approaches, FE modeling accounts

for polycrystalline microstructures without simplifying assumptions, enabling a better understanding of complex wave propagation phenomena in polycrystals, particularly the effects of multiple scattering [24]. Goshal and Turner [25] pioneered the incorporation of polycrystalline grains into an FE framework by using Voronoi tessellation and Delaunay triangulation, which are commonly used in crystallography to describe such structures [26]. This method was later validated by Shahjahan et al. [27], who examined multiple scattering in Inconel600 using a 2D Voronoi structure on FEA, which demonstrated good agreement with experimental data and therefore validating the Voronoi approach. These FEA methodologies have successfully modeled scattering phenomena in polycrystalline materials within both homogeneous and anisotropic media [24], as well as understanding the scattering between grain boundaries of adjacent grains [10]. However, there has been no investigation so far into the variation in backscattering for surface-hardened samples, which typically exhibit finer grains in the hardened layer compared to the rest of the sample. Therefore, utilising the current advancements in grain size characterisation and current finite element techniques, a method of interpreting the backscattering signal in a model constructed with two different microstructures is investigated.

In order to appropriately analyse the received backscatter signal from this model, a post processing technique of the backscattered signal must be identified. Several post processing techniques exist, which are predominantly used to identify the location of damage or defects within materials during guided wave structural health monitoring (GWSHM) [28]. A paper by Flynn et. al [29] compared the localization of seven previously reported localization method to the performance of a novel Rayleigh maximum likelihood estimate (RMLE) technique. This study realised damage as drilled holes within an aluminium cross section sample. The validity of each method was assessed by using a localizer operating characteristic (LOC). Here, the points represent a measure of probability of predicting the location of damage within concentric circles of increasing radii around the actual damage location. This indicates that each damage location has its own unique LOC, and the overall performance of the the each technique is evaluated by averaging multiple measures of LOCs. The RMLE proved superior in identifying the location of damage in the sample using LOC, verifying its effectiveness as a GWSHM localization algorithm. In the case of a microstructure difference, this method may prove useful in interpreting the backscattering signals as it transitions from microstructures with different average grain size. Therefore, this method is chosen to interpret the ultrasonic signal in the finite element analysis of the surface hardened sample in this study, in parallel with the variance method used by [20] in order to account for multiple realisations of the FE model.

1.1 Aims and Objectives

This study aims to utilise finite element method to identify the case depth of a surface hardened sample by interpreting its ultrasonic backscatter response using spatial variance and the RMLE method. The analysis is conducted based on the following objectives:

1. Generate material microstructure based on Voronoi tessellation (Section 2.1.1).
2. Assign randomly distributed grain orientation to the grains of the microstructure using Euler angles. (Section 2.1.2)
3. Construct two FE models with different grain morphologies. (Section 2.2)
4. Interpret the probability density function (PDF) and two-point correlation function (TPCF) of both models. (Section 3.1)
5. Examine the signal output of both models across N realizations and evaluate their spatial variance. Then, process this data using the RMLE method. (Section 3.2)

2 Methodology

This section provides a step-by-step outline for the finite element modelling of the polycrystalline sample in 2D. This section is separated into three parts, as shown by the flowchart in Figure 1. Section 2.1 describes how the microstructure is built from Voronoi tessellation, and how random orientation are assigned to the grains. Section 2.2 then describes how the finite element method is used on this microstructure, and a mesh convergence study to verify the validity of results. Lastly, Section 2.3 outlines the procedure for collecting the spatial variance of output signals across N realizations and employing the RMLE method to determine the case depth of the sample.

MATLAB is used as the preferred mode of analysis due to its versatility and available built in functions [30]. Furthermore, the finite element software BristolFE used for this project is an open source repository constructed by Dr Paul Wilcox, which is available for use on GitHub [31]. This software is able to perform basic static and dynamic 2D finite element simulations using a structured isometric (CPE3) mesh.

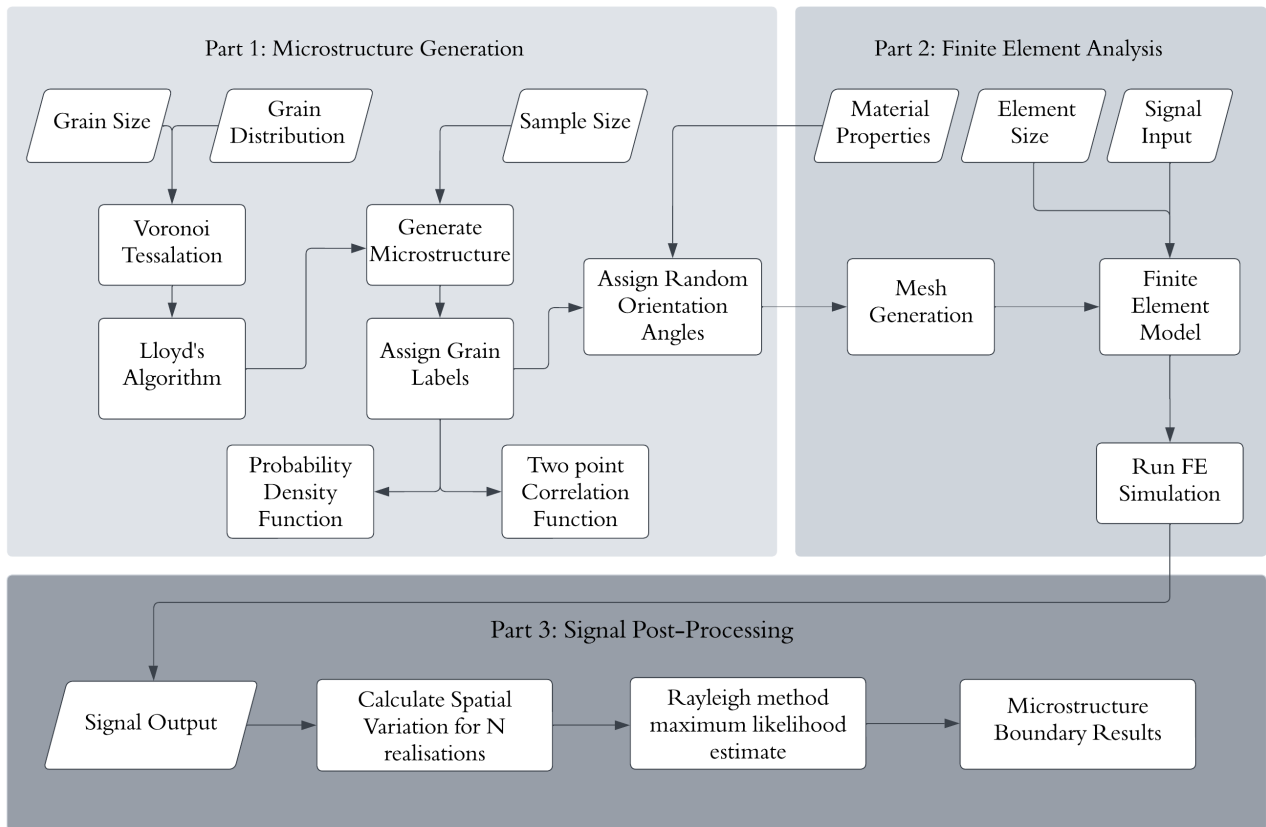


Figure 1: Process flow diagram.

2.1 Microstructure Generation

The generation of a polycrystalline microstructure for modeling purposes is commonly carried out using a Voronoi tessellation. This method partitions a plane into regions based on seed points. Each seed corresponds to a region defined as the Voronoi cell, which consists of all points closer to that seed than to any other [32]. The construction of the Voronoi tessellation to represent a microstructure involves the following steps:

2.1.1 Generating Grain Positions

The first step in generating the microstructure is generating randomly distributed seed points within the desired domain. In this study, the distribution of the seed points are based on on the input grain size and sample size as described in Section 2.2. The seed points are visualised in Figure 2a.

After specifying the seed points, the voronoi function in MATLAB [30] employs Delauney triangulation to construct the Voronoi diagram. This process transforms the initial space into regions composed of convex polygons. Each polygon encompasses the region nearest to its corresponding seed point, as illustrated in Figure 2b. These Voronoi cells are then labeled with a grain identifier in order to correlate them with their respective elements in the finite element model. The seed distribution is controlled using Lloyd's algorithm [33]. This algorithm first processes the initial set of seeds, and computes its Voronoi diagram. Then, the subsequent iterations use the centroids (C_x, C_y) of the Voronoi cells as the seed points for the next iteration. This is defined by Equation 1:

$$x'_i = C_x = \frac{1}{N_i} \sum_{j=1}^{N_i} vx_{ij}, \quad y'_i = C_y = \frac{1}{N_i} \sum_{j=1}^{N_i} vy_{ij} \quad (1)$$

Where (x_i, y_i) represents the initial position of the seed point, (x'_i, y'_i) represents the updated position after one iteration, (vx_{ij}, vy_{ij}) are the vertices of the voronoi cells representing the j-th vertex associated with the i-th input point, and N_i is the number of vertices of the voronoi cell associated with the i-th input. This algorithm is useful for controlling the uniformity of grains. The implications of iterating over the Lloyd's algorithm is discussed in Section 3.1, where the TPCF and PDF are discussed to compare two models constructed after one and five iterations of the algorithm respectively.

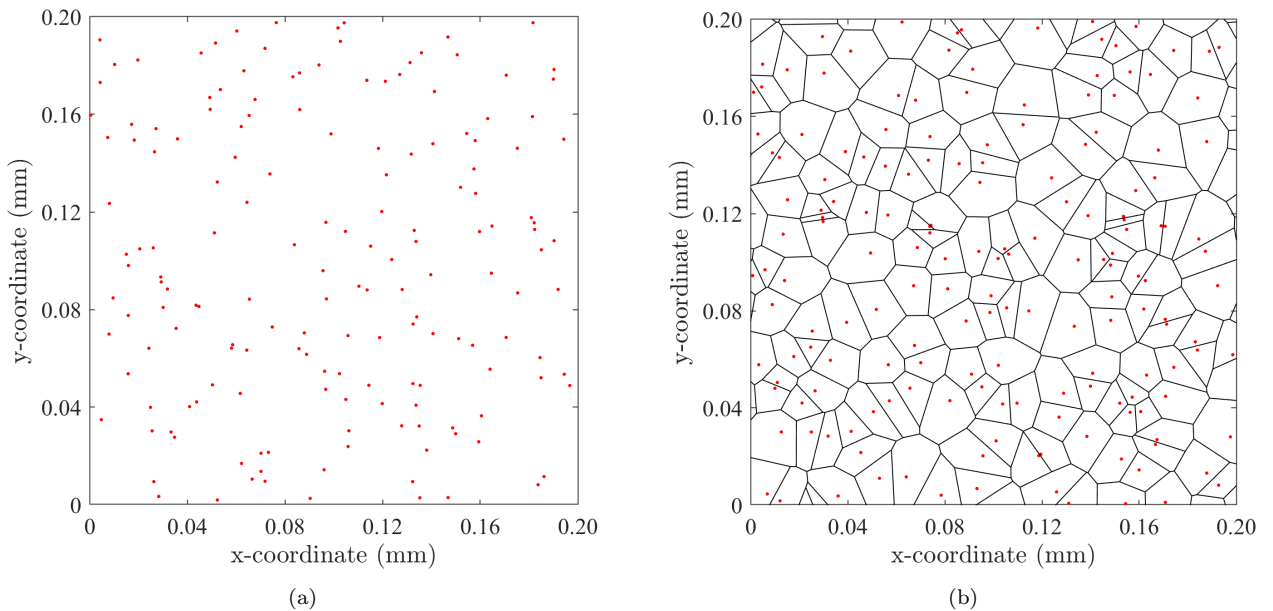


Figure 2: Illustration of the steps involved in generating polycrystal grains using voronoi tessellation: (a) randomised distribution of seed points and (b) the voronoi tessellation. The tessellation shown here used $15\mu\text{m}$ average grain size as input.

2.1.2 Assigning random orientation to grains

This step defines the process of applying material properties to each grain in the microstructure. In a polycrystalline material, each grain is oriented in three-dimensional Euclidian \mathbb{R} space relative to

sample's reference frame, which can be described by Euler angles. Every possible grain orientation in the sample must have an equal chance of occurrence in order to obtain a statistically isotropic material [21, 27]. This can be achieved by generating uniformly-distributed random roll-pitch-yaw euler angles as described by Kuffner [34], where the randomisation is based on uniform spherical sampling such that the orientations lie equally spaced on the surface of a sphere. The pseudocode used to generate the random orientation is shown in Algorithm 1, where the use of the inverse cosine relationship avoids oversampling in the polar regions [34].

Algorithm 1 Pseudocode for generating uniformly distributed Euler angles

Require: grain_label ▷ Input: Grain labels
Ensure: α, β, γ ▷ Result: Uniformly distributed Euler angles
1: $\alpha \leftarrow 2\pi \times \text{rand}(\text{length}(\text{grain_label}), 1)$
2: $\beta \leftarrow \arccos(2 \times \text{rand}(\text{length}(\text{grain_label}), 1) - 1)$
3: $\gamma \leftarrow 2\pi \times \text{rand}(\text{length}(\text{grain_label}), 1)$
4: **return** (α, β, γ)

The defined Euler angles are then used as input for orienting the grains by rotating the elasticity tensor \mathbf{C} (Equation 2) of a cubic anisotropic crystal into the rotated elastic stiffness matrix \mathbf{C}_R (Equation 3).

$$\mathbf{C} = \begin{bmatrix} C_{11} & C_{12} & C_{12} & 0 & 0 & 0 \\ C_{12} & C_{11} & C_{12} & 0 & 0 & 0 \\ C_{12} & C_{12} & C_{11} & 0 & 0 & 0 \\ 0 & 0 & 0 & C_{44} & 0 & 0 \\ 0 & 0 & 0 & 0 & C_{44} & 0 \\ 0 & 0 & 0 & 0 & 0 & C_{44} \end{bmatrix} \quad (2)$$

$$\mathbf{C}_R = \mathbf{R}_D \mathbf{C} \mathbf{R}_D^T \quad (3)$$

Where \mathbf{R}_D represents the bond transformation matrix (Equation 5). The random orientation distribution assigned to the grains is visualised using an inverse pole figure (IPF) as shown in Figure 3, with an IPF color map that show the orientation distribution in the crystallographic axis. It is evident that there is an equal distribution of orientations in each crystallographic direction as there is an even distribution of colors across the plot. This verifies that the grains exhibit isotropic behavior among the crystallographic directions denoted by $\langle 001 \rangle$, $\langle 111 \rangle$ and $\langle 011 \rangle$.

$$\mathbf{R} = \begin{bmatrix} \cos \alpha \cos \gamma - \sin \alpha \sin \gamma \cos \beta & -\cos \alpha \sin \gamma - \sin \alpha \cos \gamma \cos \beta & \sin \alpha \sin \beta \\ \sin \alpha \cos \gamma + \cos \alpha \sin \gamma \cos \beta & -\sin \alpha \sin \gamma + \cos \alpha \cos \gamma \cos \beta & -\cos \alpha \sin \beta \\ \sin \gamma \sin \beta & \cos \gamma \sin \beta & \cos \beta \end{bmatrix} \quad (4)$$

$$\mathbf{R}_D = \begin{bmatrix} R_{11}^2 & R_{12}^2 & R_{13}^2 & 2R_{12}R_{13} & 2R_{13}R_{11} & 2R_{11}R_{12} \\ R_{21}^2 & R_{22}^2 & R_{23}^2 & 2R_{22}R_{23} & 2R_{23}R_{21} & 2R_{21}R_{22} \\ R_{31}^2 & R_{32}^2 & R_{33}^2 & 2R_{32}R_{33} & 2R_{33}R_{31} & 2R_{31}R_{32} \\ R_{21}R_{31} & R_{22}R_{32} & R_{23}R_{33} & R_{22}R_{33} + R_{23}R_{32} & R_{21}R_{33} + R_{23}R_{31} & R_{22}R_{31} + R_{21}R_{32} \\ R_{31}R_{11} & R_{32}R_{12} & R_{33}R_{13} & R_{12}R_{33} + R_{13}R_{32} & R_{13}R_{31} + R_{11}R_{33} & R_{11}R_{32} + R_{12}R_{31} \\ R_{11}R_{21} & R_{12}R_{22} & R_{13}R_{23} & R_{12}R_{23} + R_{13}R_{22} & R_{13}R_{21} + R_{11}R_{23} & R_{11}R_{22} + R_{12}R_{21} \end{bmatrix} \quad (5)$$

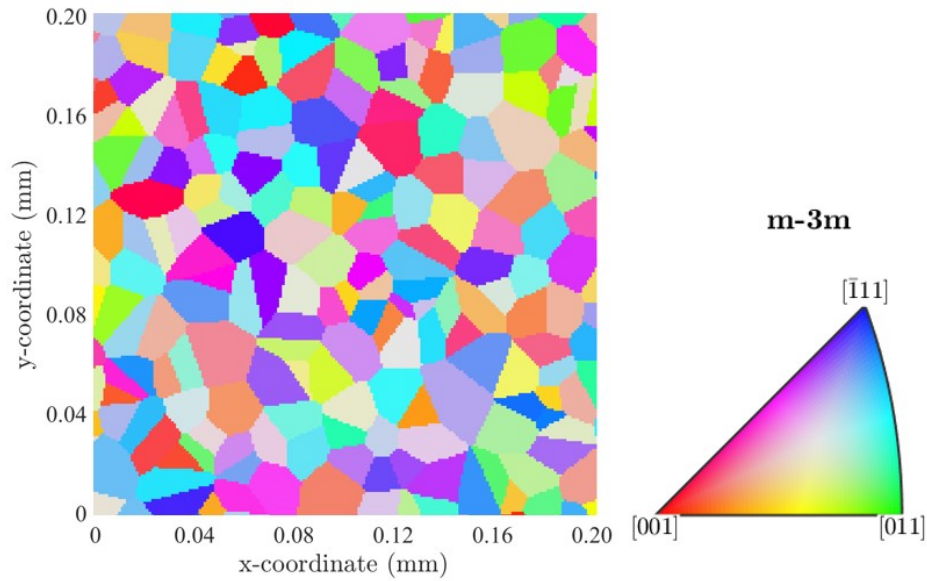


Figure 3: Illustration of the steps involved in generating polycrystal grains using voronoi tessellation: The inverse pole graph (IPF) of the oriented grains made from voronoi tessellation and the IPF color map, showing the angle distribution based on the chrystallographic axis. The tessallation shown here used $15\mu\text{m}$ average grain size as input.

2.2 Finite Element Model

The steps explained in Section 2.1 are not built in functions on BristolFE [31] and were therefore encoded into this software in a collaboration between the author and Dr. Jie Zhang, in order to extend its functionality into processing models with microstructural grains.

2.2.1 Experimental Set-Up

For this initial investigation, a relatively small sample size is used in order to optimise processing time during testing. The test set-up, shown in Figure 4, is a 2D sample with a 6mm depth and 1.5mm width. To simulate a surface hardened sample, the microstructure, from a depth of 0 to 2.5mm as shown in Figure 4, will consist of grains with a $15\mu\text{m}$ average grain size, indicated by G1. The rest of the sample, as separated by the dotted line in Figure 4 will consist of a microstructure with average grain size of $30\mu\text{m}$, indicated by G2.

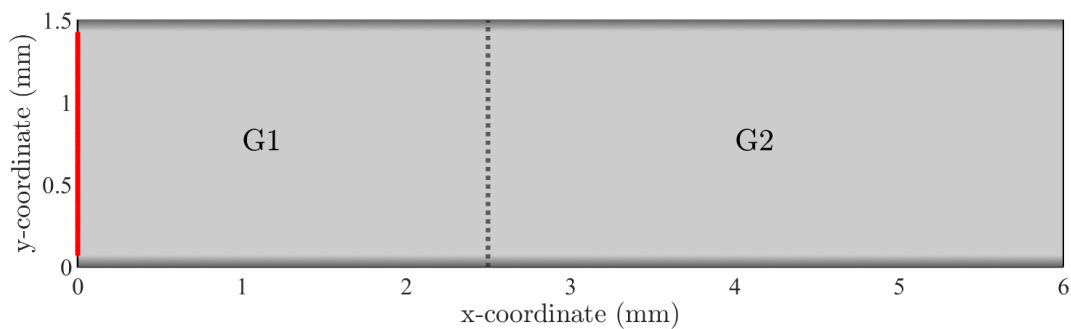


Figure 4: FE model of a 6x1.5mm surface hardened stainless steel sample. The red line represents the source of the ultrasonic signal, and the grey shadows along the depth of the sample represent the absorbing boundary layer. The dotted line at 2.5mm represents the boundary between the different microstructures, labelled as G1 and G2. This is the same configuration applied to both Models 1 and 2.

Two models are constructed: Model 1 (M1) consists of grains with a distribution based on one iteration of lloyd's algorithm, and Model 2 (M2) consists of grains generated based on five iterations. Both models are valid approximations of real polychrystalline materials. Model 1 exhibits a log-normal

grain size distribution commonly observed in polychrystalline materials, and Model 2 exhibits more a more uniform distribution, which are evident in well-annealed structures [22]. The distribution of grains in Model 1 & 2 are visualised in Figure 5.

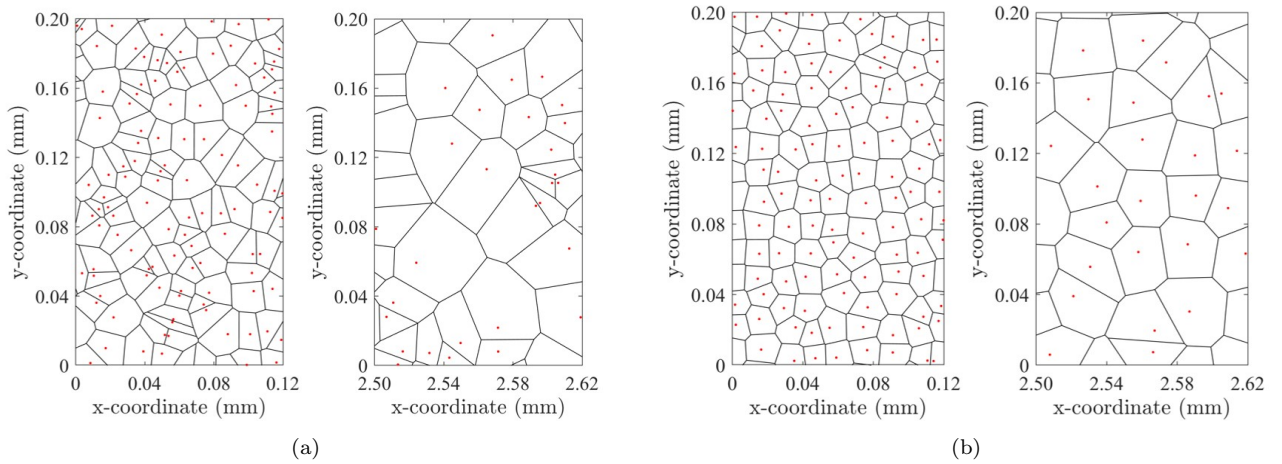


Figure 5: The grain size distribution for (a) Model 1 and (b) Model 2. This shows a close up image of the grains in Figure 4, relating to both G1 and G2 in both models based on their x-coordinate.

Using the grain identifier described in Section 2.1.1, the grains are discretized using a structured isometric mesh (CPE3) on BristolFE [31]. An absorbing boundary layer is applied on the boundaries of the sample adjacent to the path of the ultrasound, represented by the grey shadow on the edge of the sample in Figure 4. This is to minimise the backscattering from these walls, and is also applied in several other FE studies to simulate an infinitely wide sample [25]. The ultrasonic signal is applied from source points along the nodes of the sample at (0,0), spanning the whole width of the sample. The excitation is a three cycle, 10MHz, Gaussian-windowed pulse, which leads to an average wavelength of $530 \mu\text{m}$ for the specified material. This frequency was chosen as based on findings by Du et. al [20], who demonstrated that the frequency range of 10-20 MHz resulted in the greatest sensitivity to the microstructure in their steel railroad wheel sample. The lowest value in this range was utilized to ensure the largest element per wavelength ratio, ensuring accurate representation of wave behavior and improved numerical stability in FEA [24].

Table 1 lists the material properties used in the FE model. Stainless Steel is selected due to its versatility and applications as a surface hardened material, with several studies [35–37] confirming these properties. All material properties used are sourced from EduPack [38].

Table 1: Material properties used to represent Stainless Steel [38].

Material	Density (kg/m^3)	Elastic Constants (GPa)		
		C_{11}	C_{12}	C_{44}
Stainless Steel	7870	204.6	137.7	126.2

2.2.2 Mesh Convergence

A mesh convergence study was performed to ensure successful simulation of grain scattering behavior and wave propagation within the sample [24]. This study was conducted similar to Van Pamel et al. [21], who investigated the effects of the number of elements per grain dimension using two metrics to measure convergence: centre frequency attenuation and group velocity. In this study, the signal amplitude and time of flight difference is measured instead for simplicity. The first metric is measured

by calculating the difference between the peak amplitude of the received time-domain Hilbert envelope A and the peak of the converged solution, A_c , taken from the highest available mesh density. The second metric is measured similarly: the time of flight t is calculated based on the peak of the Hilbert envelope and is compared with that of the converged solution t_c . These measurements are visualised in Figure 6a.

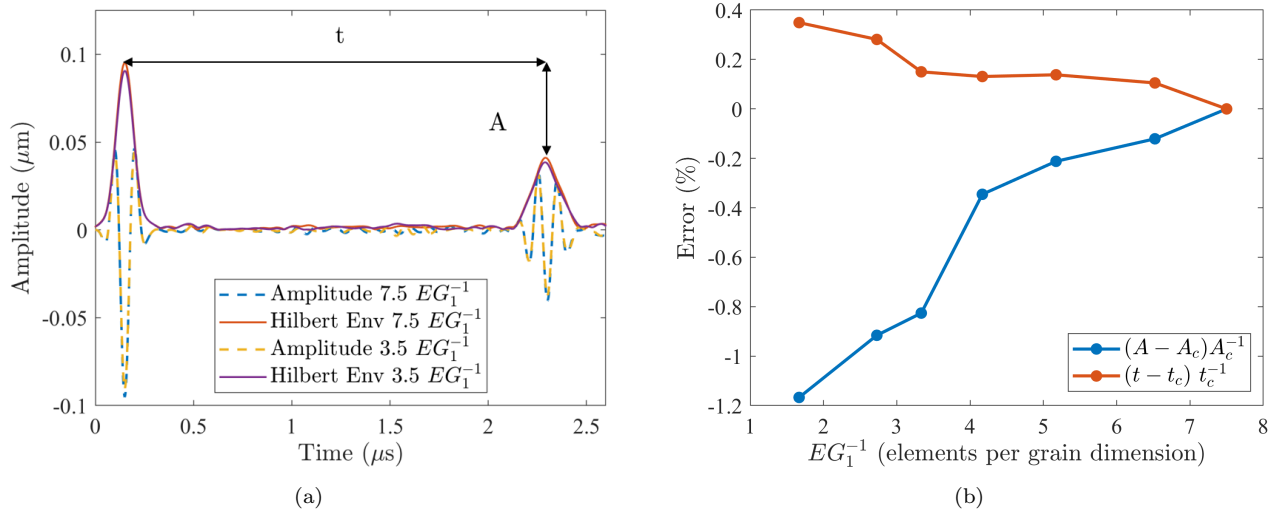


Figure 6: (a) The received signal for models with 3.5 and 7.5 elements per grain which was used to calculate the convergence metrics described. This also shows how the convergence metrics are measured. Note that only two models are shown here for clarity. (b) Convergence of normalised amplitude and time of flight against elements per grain.

Figure 6b shows the plot of elements E per grain dimension G_1 against the normalised error of the two metrics described. As the model consists of 2 different grain sizes, the elements per grain measure is based on the smaller of the two, $G_1 = 15 \mu\text{m}$. Figure 6a shows the received signals for different elements per grain values.

The progress of convergence for both metrics align closely with the findings by Van Pamel et al. [21], who described that the convergence for a structured mesh occurs more monotonically than in other mesh types (i.e. unstructured mesh). Both metrics also display similar error values calculated in [21] for a structured isometric mesh on grains of size $100 \mu\text{m}$.

Generally, a ratio of 10 elements per grain dimension is accepted as converged in several studies [24, 27]. However, due to high computational costs for finer mesh densities, the highest available mesh metric was 7.5 elements per grain. Nevertheless, the use of a coarser mesh is valid based on the findings of Van Pamel et al. [21]. In their study, the model with grain sizes of $100 \mu\text{m}$ converges quicker than that of models with $250 \mu\text{m}$ and $500 \mu\text{m}$ grains. This behavior was explained by the interaction between grain scattering and mesh scattering. In models with smaller grains, the wavelength to grain size ratio is larger, therefore there is lower grain scattering induced attenuation in the model. This also explains that if the model had a coarser mesh, it would also demonstrate similar levels of attenuation. Furthermore, their mesh convergence study showed that for their $100 \mu\text{m}$ model with a structured mesh, convergence within 1% error is achieved at approximately 3 elements per grain size dimension, similar to the findings in this mesh convergence. Nevertheless, the highest available mesh density is still used to analyse the sample, as it provides a more accurate representation of the variation in grain geometry and impedance variations [27]. The mesh density of 7.5 elements per grain dimension, which corresponds to element size $2 \mu\text{m}$, is shown in Figures 7a and 7b for Model 1 and 2 respectively.

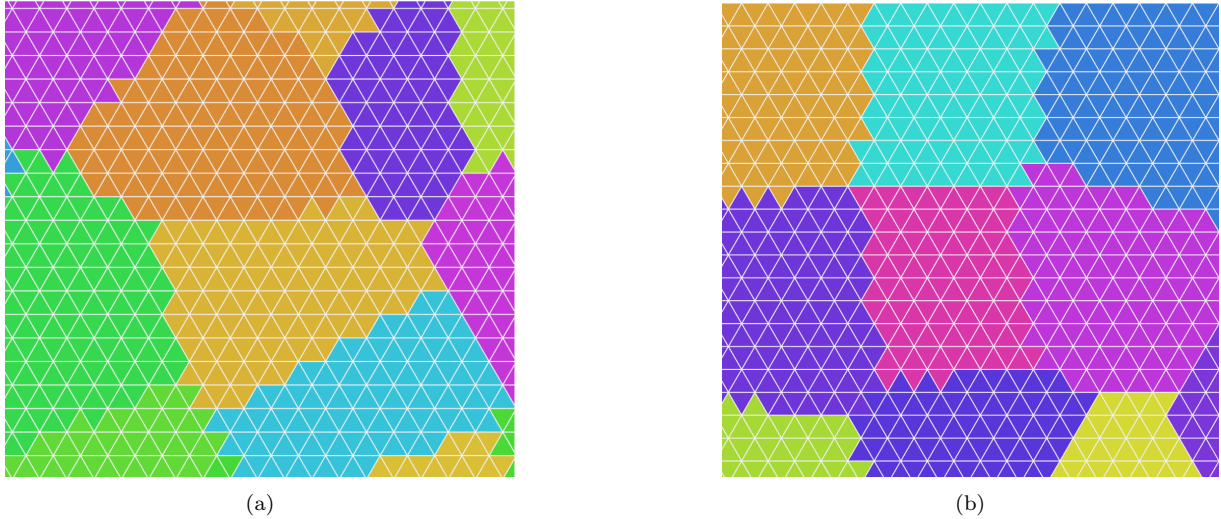


Figure 7: Close-up view of the mesh applied to the G1 region (grain size of $15 \mu\text{m}$) in both (a) Model 1 and (b) Model 2.

2.3 Signal Processing

This section provides an overview of the RMLE method as proposed by Flynn et. al. [29] and a description of how spatial variance for N realisations is utilised within this method.

2.3.1 Rayleigh Maximum Likelihood Estimate

The maximum likelihood estimation technique has been widely used in different statistical studies as a method of measuring parameters [39]. This technique searches different possible population values and derives the parameter estimates that are most likely to accurately represent the observed sample data. This technique was employed by Flynn et al [29], who described that if damage is centered at some location \mathbf{x} , the feature matrix (observed sample data) will follow some model " $\mathbf{V} = f(\mathbf{x})$ ", parametrised by the damage location. Therefore, it will follow some likelihood function " $L(\mathbf{x}|\mathbf{V})$ ", where the estimated damage location is when \mathbf{x} is at a maximum within the likelihood function, assuming that \mathbf{x} is the only unknown parameter. However, they explained that when damage is present, there is disturbance within the signal received. The received waveform can therefore be divided into two sections (i) the time before the arrival of any scatter from the damage and (ii) the arrival of a scattered waveform due to changes in the structure's geometric features. Therefore, the likelihood is dependent on three unknown parameter vectors: $L(\hat{\sigma}_1, \hat{\sigma}_2, \mathbf{x}|\mathbf{V})$, where $\hat{\sigma}_1, \hat{\sigma}_2$ are Rayleigh parameters representing the two sections of the wave described. The divided sections of the waveform can be broken into two parts according to Equation 6.

$$\left. \begin{aligned} f(\hat{\sigma}_1(\eta)), \text{ for } n = 1, \dots, \eta \\ f(\hat{\sigma}_2(\eta)), \text{ for } n = \eta + 1, \dots, N \end{aligned} \right\} \quad (6)$$

In the present study, the same concept can be utilised for a surface hardened sample. The boundary between G1 and G2 can be located at some location \mathbf{x} with correlated index η along the depth of the sample, and the microstructural variations before and after the boundary can represent the Rayleigh parameters. This assumption is valid, as the unified theory [12] confirms that wave scattering depends on factors such as microstructural variations. The test statistic $I(\mathbf{x}) = L(\hat{\sigma}_1, \hat{\sigma}_2, \mathbf{x}|\mathbf{V})$ in the RMLE method is given in Equation 7 as a function of the boundary location \mathbf{x} :

$$I(\mathbf{x}) = 2 \sum_{n=1}^N (\log(\nu[n])) - \eta \log \hat{\sigma}_1^2(\eta) - (N - \eta) \log \hat{\sigma}_2^2(\eta) - N \quad (7)$$

$$\hat{\sigma}_1(\eta) = \sqrt{\frac{1}{2(\eta)} \sum_{n=1}^{\eta} \nu^2[n]} \quad \hat{\sigma}_2(\eta) = \sqrt{\frac{1}{2(N-\eta)} \sum_{n=\eta+1}^N \nu^2[n]} \quad (8)$$

Where N is the total number of recorded signal data, n represents the time step of the data, ν represents the amplitude waveform data received as output from the FE analysis or calculated spatial variance (described in Section 2.3.2), and $\sigma_1(\eta), \sigma_2(\eta)$ are the Rayleigh parameters (Equation 8). Note that Equations 7, 8 are derived in Flynn et al.'s study [29] and are therefore not fully derived in this study.

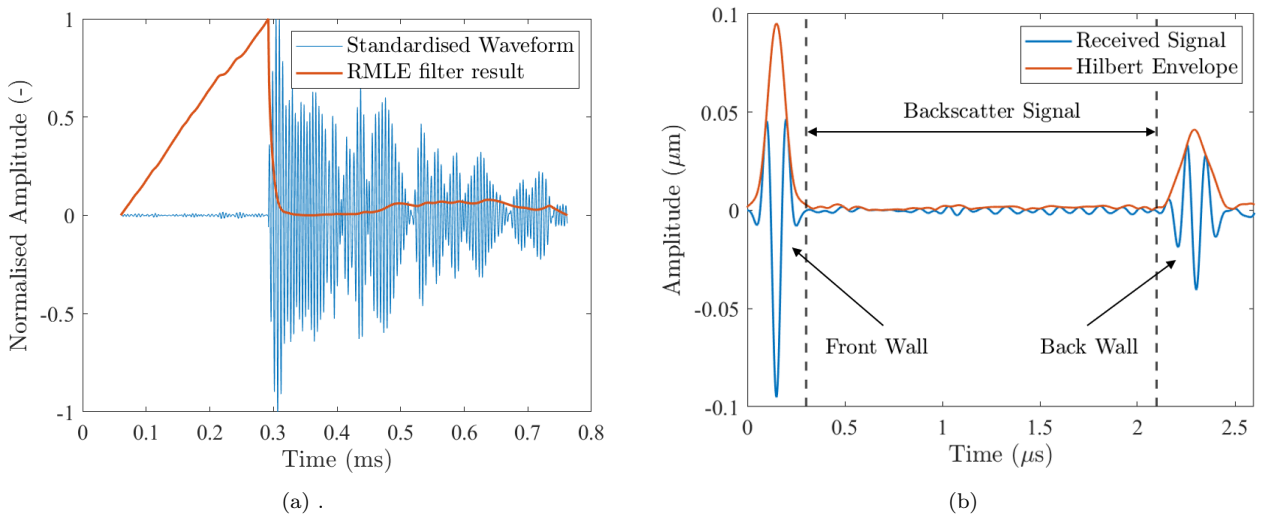


Figure 8: (a) Standardised waveform and its RMLE filter result. Note that this signal is unrelated to the results in this study and is used for demonstrative purposes only. (b) Example of a received signal from an FEA run, demonstrating how the signal is sectioned such that the region of interest is processed by the RMLE.

Figure 8a shows an example of how the test statistic used in the RMLE method can be interpreted. The blue signal shows the recorded wave data, and the orange line represents the filter results based on Equation 7. As described, it can be seen that the maximum $I(x)$ is when there is a change in the consistency of the received signal.

2.3.2 Spatial Variance

In order to account for multiple realisations of Models 1 and 2, a time-dependent spatial variance model is used to process the results for a number of model realisations, as utilised by Du et al. [20]. The spatial variance defines the statistical expectation regarding the variability of ultrasonic measurements made from different realisations of on the sample, which in theory, should provide a better representation of results for an increasing number of realisations. The spatial variance of the acquired backscatter signals is defined in Equation 9:

$$\Phi(t) = \frac{1}{N} \sum_{i=1}^N (U_i(t) - b(t))^2 = [U^2] - [U]^2 \quad (9)$$

Where N is the number of realisations, $b(t)$ is the group average of the backscatter signals, $[U^2]$ is the group average of the squared backscatter signals and $[U]^2$ is the square of the mean backscatter signals. The BristolFE software described in Section 2.2 records the displacement history at each node on the excitation line source of the sample shown in Figure 4. The region of interest for interpreting the backscattering lie between the front wall and backwall echoes, which are the regions where a spike in the signal is evident, as shown in Figure 8b. The signals received from each realisation is trimmed to remove the front wall and back wall echoes, and are subsequently processed using Equation 9. The spatial variance $\Phi(t)$ is then used as ν in Equation 7, in order to calculate the maximum likelihood estimate over a number of realisations.

3 Results & Discussion

This section presents and evaluates the results of the finite element analysis and signal processing for Models 1 and 2. 20 realisations for each model were ran with a mesh density of 7.5 elements per grain. This produced 5211360 elements, with each realisation taking approximately 8-10 hours to complete. Each realisation produced a different microstructure layout, to ensure that various configurations are recorded. Recording multiple realisations is ideal in this scenario as more statistics can be deduced and thus providing better comparison with experimental data. Figure 9 shows a representation of a model, which illustrates how the grains are proportioned compared to the model.

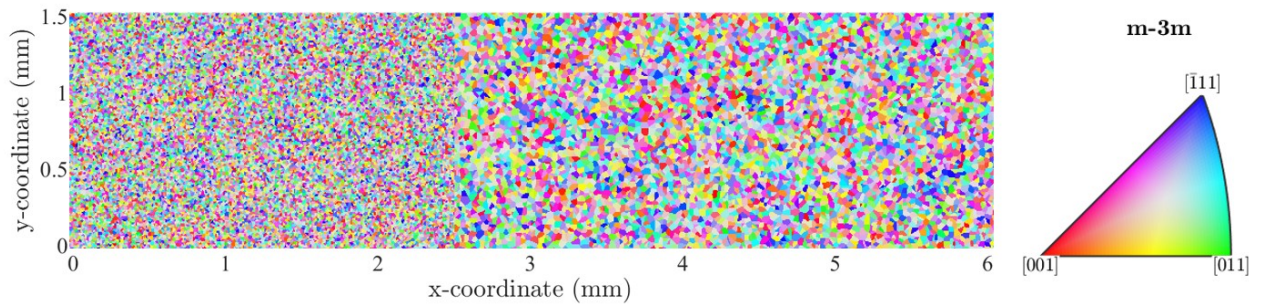


Figure 9: IPF of the modelled stainless steel sample for FEA. The grains from 0-2.5mm signify $G1 = 15\mu\text{m}$ and the grains from 2.5mm-6mm signify $G2 = 30\mu\text{m}$.

3.1 Two-point Correlation Function & Probability Density Function

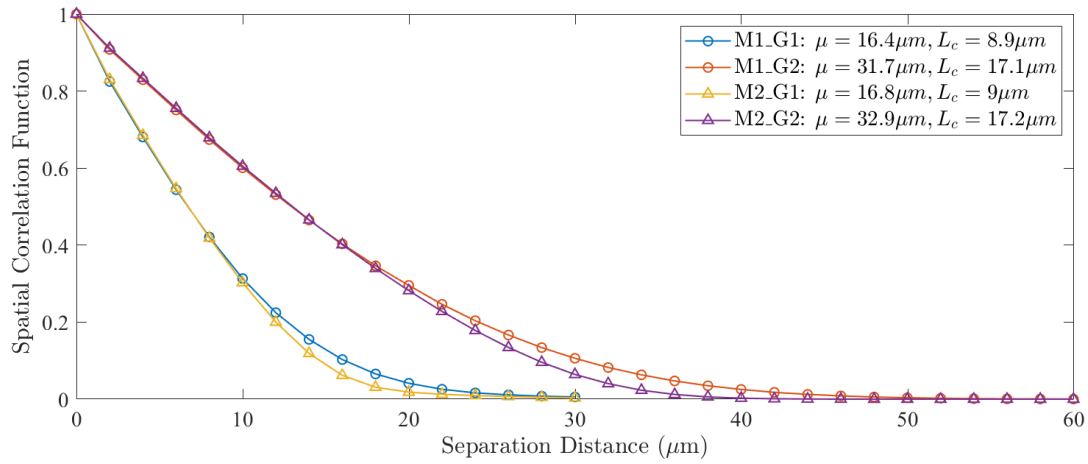
The two-point correlation function (TPCF) and probability density function (PDF) are utilised in order to understand how geometrical variations may influence the results of the FE analysis. When the microstructure grains are segmented into elements for FE model, their average grain sizes deviate from the input grains defined due to discretization. Therefore, a summary of the input and output statistics are provided in Table 2, averaged over the 20 realisations in both Model 1 and 2. It can be seen that the output mean grain size for all ensembles are roughly 10% greater than the input sizes specified.

The two-point correlation function $W(r)$ is defined as the probability that two points, which are separated by the vector r , are located within the same domain [10]. It provides information about the average distance over which neighbouring points exhibit correlated properties, i.e if they belong to the same grain. In this study, the TPCF is calculated by using a segmented image of the sample, where elements composing a grain are labelled with an identifier for correlation with other elements within the same grain. 10^6 random pairs of points are generated within the image: (i) a random point and (ii) another random point separated from (i) at a distance r . The $r(j)$ values represent

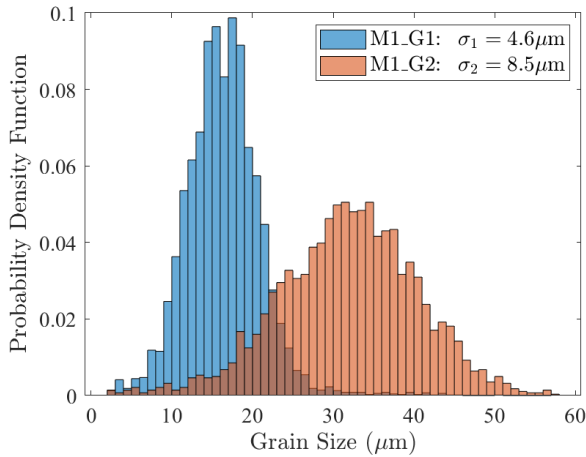
separation distances with a step size of one element. The correlation $W(r)$ is determined for each r value and is plotted for Models 1 and 2 in Figure 10a.

Table 2: Microstructural information relating to the grains in Model 1 and 2. The output values are the average of 20 realisations in each Model. μ and σ are the mean and standard deviation of the grain size, respectively. L_C represents the characteristic length for each parameter.

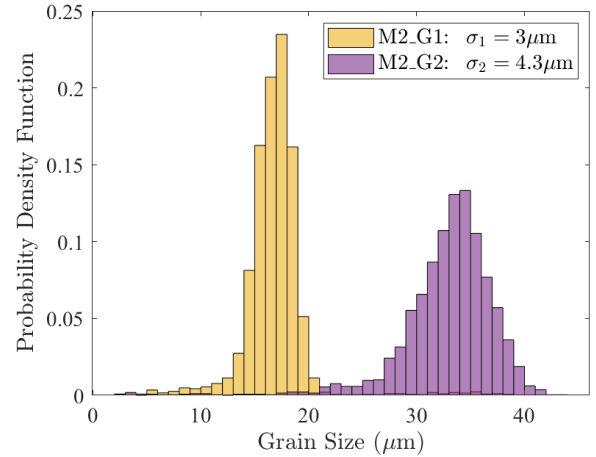
Model	Ensemble	Input Statistics		Output Statistics			
		Grain size	No. of Iterations	$\mu(\mu\text{m})$	$\sigma(\mu\text{m})$	L_C	No. of Grains
1	M1_G1	15	1	16.4	4.6	8.9	16990
1	M1_G2	30	1	31.7	8.5	17.1	6040
2	M2_G1	15	5	16.8	3.0	9.0	16960
2	M2_G2	30	5	32.9	4.3	17.2	6020



(a)



(b)



(c)

Figure 10: (a) Two-point correlation function against separation distance. Note that L_C signifies the correlation length when the curve decays to 0.1. (b) Grain Size distribution for Model 1 and (c) Model 2.

The correlation function $W(r)$ is theoretically represented as an exponential function using a correlation length L which corresponds with the mean grain radius r , such that $W(r) = e^{-r/L}$. Therefore, microstructures that have similar mean grain diameter but different standard deviations will show comparable TPCF trends. This is evident on figure 10a, where it can be seen that G1 and G2 in both

samples show similar TPCF curves. The characteristic length L_C in Figure 10a and Table 2 refers to the distance where the TPCF curve decays to 0.1, corresponding to the characteristic length scale where correlation between the grains become negligible. Model 1 exhibits slightly longer correlation lengths due to the broader distribution of grains in this model, consistent with the observations by Ryzy et al. [23].

These results are analogous with Figures 10b and 10c, which illustrates the probability density function for Models 1 and 2 respectively. It is noticeable that there is a greater overlap between G1 and G2 grain sizes in Model 1, with 23% of grain sizes shared between them. This distribution influences the FE results because ultrasonic scattering is governed by microstructural variations [23]. Consequently, Model 1 is anticipated to have a larger spatial variance compared to Model 2, where only 3% of grain sizes are shared between G1 and G2.

3.2 Signal Processing Results

The results of the RMLE analysis is shown in Figures 11a and 11b for Model 1 and 2 respectively. It is apparent that the spatial variance among the realisations in Model 1 is more varied compared to Model 2, which align with the larger variations in grain sizes observed in this model. In Model 2, a spike in spatial variance can be observed around the 2.5mm region, in contrast to the more scattered trend evident in Model 1. These observations are consistent with the variance seen in the experimental setup by Du et al. [20] for a quenched steel railroad wheel. They observed that the spatial variance decreases near the tread surface of the quenched sample due to the fine lamellar spacing of pearlite, in contrast to the lack of spike in the unquenched sample. This demonstrates that microstructural variations affect ultrasonic scattering, which align with the results from this FE analysis.

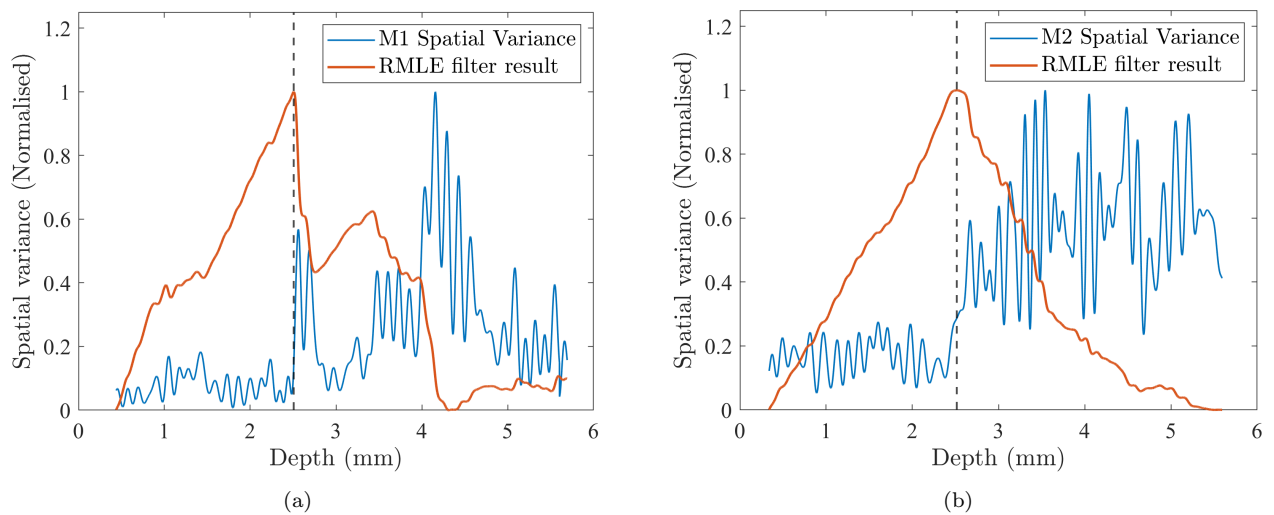


Figure 11: RMLE Results for 20 realisations of (a) Model 1 and (b) Model 2 respectively. The dotted line signifies the depth at which the RMLE curve peaks, which is within 1% of the modelled boundary layer at 2.5mm for both models.

Both Figures 11a and 11b, which are based on 20 realisations, provide a good estimate of the region where the sample transition from G1 to G2 using the RMLE method. In both Models 1 and 2, this predicted region is within 1% of the actual transition between G1 and G2. The RMLE curve for Model 2 exhibits a smoother trend dictated by the more uniform grains evident in this model. The benefit of using the RMLE method in this scenario is that it provides a clearer image the trend in the

waveform. It is not exactly clear in Model 1 where there is a change in the spatial variance waveform, therefore this method is especially suited for structures with more complex forms of scattering.

Figures 12a and 12b provide the peak RMLE curve for different numbers of realisations. This comparison involved executing various combinations of realisations randomly at N number of realisations and recording the peak of the RMLE curve for each. It is evident that Model 2 converges more rapidly to the actual boundary at 2.5mm, achieving approximately 10% accuracy after 8 realizations. The wider range of estimates for Model 1 can be attributed to the broader distribution of grain sizes compared to Model 2. Another potential factor affecting this trend is noise. According to Flynn et al [29], the RMLE is sensitive to noise as it relies heavily on the sharpness and magnitude of the 'jump' in the Rayleigh parameter (between $\hat{\sigma}_1$ and $\hat{\sigma}_2$). This means that noise reduces the accuracy of the RMLE by reducing the prominence of the peak where there is a transition in the waveform. While the signals are uniformly trimmed at the same position for all cases as explained in Section 2.3.2, differences in microstructures may introduce varying distribution noise from the back wall and front wall. These results further validate the use of the spatial variance to analyse multiple realisations, as it can be seen that there is a larger range of predicted boundary location between G1 and G2 at one realisation.

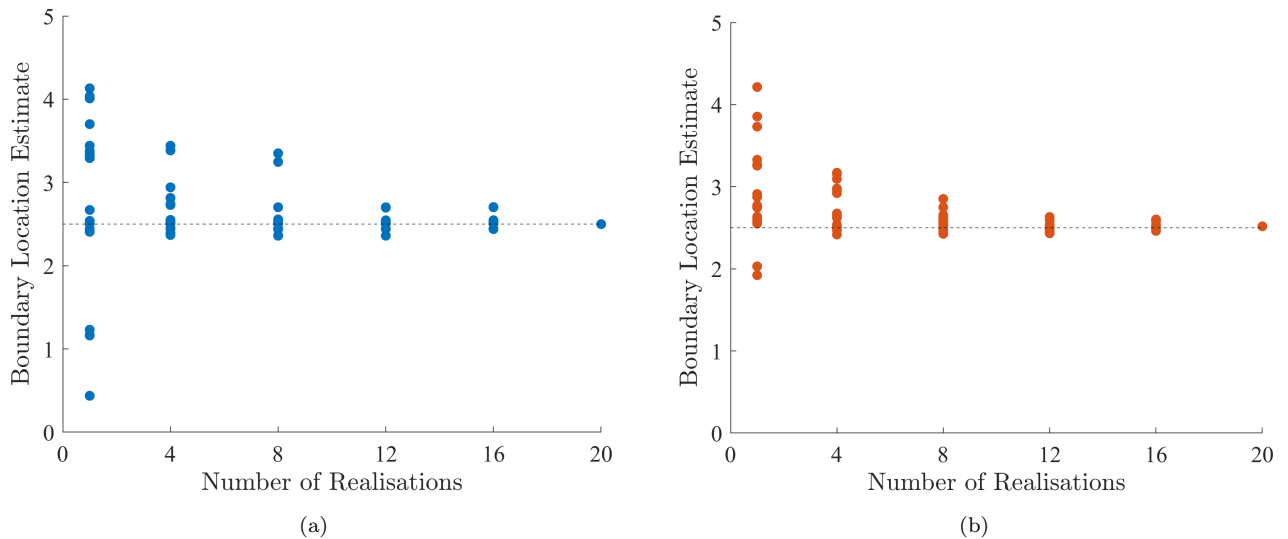


Figure 12: RMLE convergence for (a) Model 1 and (b) Model 2 respectively. This displays the range of predicted boundary locations based on random combinations of realisations.

4 Conclusion

This study explores the ultrasonic backscattering from a surface-hardened sample through finite element analysis, employing a novel maximum likelihood estimation process to process the output signal. Two 2D models representing surface-hardened steel samples are constructed to investigate the effects of grain size distribution and uniformity on the analysis results, with Model 1 and Model 2 undergoing Lloyd's algorithm once and five times, respectively. This study employs a method referred as RMLE which calculates maximum likelihood considering Rayleigh parameters that divide the signal into two distinct sections ($\hat{\sigma}_1$ and $\hat{\sigma}_2$). This method was used in conjunction with the spatial variance across 20 realisations of the two models, to capture more accurate results. The results indicate a correlation between grain size distribution and signal scattering, confirming that this model adheres to the unified theory [12] and aligns with similar studies [20, 21]. The RMLE successfully estimates the boundary location between the two microstructures G1 and G2 in both

samples to 1% accuracy. The results suggest that using relatively simple estimations of experimental setups, such as employing 2D FE analysis, is a viable approach that yields reasonable results. Overall, the progress and insights outlined in this study aim to contribute to the continuous improvement of FE simulations for ultrasonic NDE of polycrystalline materials and signal processing techniques.

4.1 Further Work

This study holds broad practical applications due to the variety of treatment processes in materials that result in different grain morphologies. While this preliminary study concentrated on a surface-hardened sample, there remains significant scope for further analysis in this area:

- **Experimental comparison:** This study can be extended by comparing the results collected to an experimental set-up of the surface hardened steel sample. This procedure can be implemented with 2 possible configurations. A sample can be constructed using 3D printing to capture the microstructural differences in G1 and G2. Another approach is to utilise a surface hardened sample with a known case depth and hardening process as this contributes to the grain morphology in the sample. A transducer can be set at a number of spatial positions on the sample, where the signals obtained at each position can be processed using the spatial variance and RMLE method. Due to time constraints, these experiments were not conducted for comparison, however these techniques would be useful for further validation of this model.
- **Transition zone modelling:** In this study, the boundary between G1 and G2 is realised as an abrupt change in the sample, with no transition zone depth. In practice, surface hardened samples exhibit a transition zone where the microstructure gradually shifts to a different grain morphology [2]. Another FEA study can be conducted where a transition zone is modelled, to capture how this influences the resulting spatial variance and RMLE result.
- **Analyses with different parameters:** In the present study, the inputs to the model were limited to grain sizes in G1 and G2 at 15 μm and 30 μm respectively due to time constraints. Several further FEA studies can be conducted with varying G1 and G2 sizes in order to capture more complex grain morphologies. There is also a possibility of reducing the difference between G1 and G2 to find the minimum difference between the microstructures which still present reasonable spatial variance between the two. Furthermore, it would also be beneficial to test a range of ultrasonic frequencies to compare the behavior each have on the backscattering. Another potential approach is to conduct an FEA study without an absorbing boundary layer, which could provide a more realistic comparison to experimental setups by introducing backscattering noise effects. Although this method would require additional signal filtering before processing with spatial variance and the RMLE method, it could offer valuable insights into how noise influences backscattering signals.
- **Utilising efficient software:** In this study, utilising an element size of 7.5 grains per element led to a model completion time of approximately 9 hours. This was a significant constraint in the study, as it would have been preferable to conduct more than 20 realizations per model. Other studies have utilized alternative software, such as Pogo [21] and Neper [23], for simulating microstructural grains, which may offer improved capabilities for running such structures. Additionally, both of these software options offer 3D capabilities and various mesh types, allowing for more varied analyses to be conducted.

References

- [1] Joseph R Davis. *Surface hardening of steels: understanding the basics*. ASM international, 2002.
- [2] Meysam Naghizadeh and Hamed Mirzadeh. Effects of grain size on mechanical properties and work-hardening behavior of aisi 304 austenitic stainless steel. *Steel research international*, 90(10):1900153, 2019.
- [3] RL Cryderman, E Arterbury, and F Bamrud. Effects of initial microstructure and induction heating cycle on the microstructure and torsional fatigue performance of a steel containing 0.6 wt pct carbon. *Journal of Materials Engineering and Performance*, pages 1–14, 2023.
- [4] Vahid Javaheri, Satish Kolli, Bjørnar Grande, and David Porter. Insight into the induction hardening behavior of a new 0.40% c microalloyed steel: Effects of initial microstructure and thermal cycles. *Materials Characterization*, 149:165–183, 2019.
- [5] C Revilla, B López, and JM Rodriguez-Ibabe. Carbide size refinement by controlling the heating rate during induction tempering in a low alloy steel. *Materials & Design (1980-2015)*, 62:296–304, 2014.
- [6] R Velazquez-Hernandez, A Melnikov, A Mandelis, K Sivagurunathan, ME Rodriguez-Garcia, and J Garcia. Non-destructive measurements of large case depths in hardened steels using the thermal-wave radar. *NDT & E International*, 45(1):16–21, 2012.
- [7] Sebastian Send, Dominik Dapprich, James Thomas, and Lasse Suominen. Non-destructive case depth determination by means of low-frequency barkhausen noise measurements. *Journal of Nondestructive Evaluation*, 37(4):82, 2018.
- [8] Farhang Honarvar and Mehdi Zeighami. Application of signal processing techniques to case depth measurements by ultrasonic method. In *Proceedings of the 17th World conference on nondestructive testing, Shanghai, China*, pages 25–28, 2008.
- [9] R Baqeri, F Honarvar, and R Mehdizad. Case depth profile measurement of hardened components using ultrasonic backscattering method. In *18th World conference on nondestructive testing, Durban, South Africa*, pages 16–20, 2012.
- [10] Musa Norouzian, Showmic Islam, and Joseph A Turner. Influence of microstructural grain-size distribution on ultrasonic scattering. *Ultrasonics*, 102:106032, 2020.
- [11] Warren P Mason and HJ McSkimin. Attenuation and scattering of high frequency sound waves in metals and glasses. *The Journal of the Acoustical Society of America*, 19(3):464–473, 1947.
- [12] Fred E Stanke and Gordon S Kino. A unified theory for elastic wave propagation in polycrystalline materials. *The Journal of the Acoustical Society of America*, 75(3):665–681, 1984.
- [13] Stanislav Rokhlin, Dale Chimenti, and Peter Nagy. *Physical ultrasonics of composites*. Oxford University Press, 2011.
- [14] Yousif Humeida, Paul D Wilcox, Michael D Todd, and Bruce W Drinkwater. A probabilistic approach for the optimisation of ultrasonic array inspection techniques. *Ndt & E International*, 68:43–52, 2014.
- [15] Long Bai, Alexander Velichko, and Bruce W Drinkwater. Grain scattering noise modeling and its use in the detection and characterization of defects using ultrasonic arrays. *IEEE Transactions on Ultrasonics, Ferroelectrics, and Frequency Control*, 66(11):1798–1813, 2019.
- [16] Goutam Ghoshal, Joseph A Turner, and Richard L Weaver. Wigner distribution of a transducer beam pattern within a multiple scattering formalism for heterogeneous solids. *The Journal of the Acoustical Society of America*, 122(4):2009–2021, 2007.
- [17] Goutam Ghoshal and Joseph A Turner. Diffuse ultrasonic backscatter at normal incidence through a curved interface. *The Journal of the Acoustical Society of America*, 128(6):3449–3458, 2010.
- [18] Jie Zhang, Yongfeng Song, Xiongbing Li, and ChengHuan Zhong. Comparison of experimental measurements of material grain size using ultrasound. *Journal of Nondestructive Evaluation*, 39(2):30, 2020.
- [19] J Li, L Yang, and SI Rokhlin. Effect of texture and grain shape on ultrasonic backscattering in polycrystals. *Ultrasonics*, 54(7):1789–1803, 2014.
- [20] Hualong Du, Cameron Lonsdale, John Oliver, Brent M Wilson, and Joseph A Turner. Evaluation of railroad wheel steel with lamellar duplex microstructures using diffuse ultrasonic backscatter. *Journal of Nondestructive Evaluation*, 32:331–340, 2013.

- [21] Anton Van Pamel, Colin R Brett, Peter Huthwaite, and Michael JS Lowe. Finite element modelling of elastic wave scattering within a polycrystalline material in two and three dimensions. *The Journal of the Acoustical Society of America*, 138(4):2326–2336, 2015.
- [22] S Shivaprasad, CV Krishnamurthy, and Krishnan Balasubramaniam. Modeling and simulation of ultrasonic beam skewing in polycrystalline materials. *International Journal of Advances in Engineering Sciences and Applied Mathematics*, 10:70–78, 2018.
- [23] Martin Ryzy, Tomáš Grabec, Petr Sedlák, and István A Veres. Influence of grain morphology on ultrasonic wave attenuation in polycrystalline media with statistically equiaxed grains. *The Journal of the Acoustical Society of America*, 143(1):219–229, 2018.
- [24] Xue Bai, B Tie, J-H Schmitt, and D Aubry. Finite element modeling of grain size effects on the ultrasonic microstructural noise backscattering in polycrystalline materials. *Ultrasonics*, 87:182–202, 2018.
- [25] Goutam Ghoshal and Joseph A Turner. Numerical model of longitudinal wave scattering in polycrystals. *IEEE transactions on ultrasonics, ferroelectrics, and frequency control*, 56(7):1419–1428, 2009.
- [26] Sriram Ganesan, Iman Javaheri, and Veera Sundararaghavan. Constrained voronoi models for interpreting surface microstructural measurements. *Mechanics of Materials*, 159:103892, 2021.
- [27] S Shahjahan, F Rupin, A Aubry, B Chassignole, T Fouquet, and A Derode. Comparison between experimental and 2-d numerical studies of multiple scattering in inconel600® by means of array probes. *Ultrasonics*, 54(1):358–367, 2014.
- [28] Ajay Raghavan. *Guided-wave structural health monitoring*. PhD thesis, 2007.
- [29] Eric B Flynn, Michael D Todd, Paul D Wilcox, Bruce W Drinkwater, and Anthony J Croxford. Maximum-likelihood estimation of damage location in guided-wave structural health monitoring. *Proceedings of the Royal Society A: Mathematical, Physical and Engineering Sciences*, 467(2133):2575–2596, 2011.
- [30] MathWorks. *MATLAB Handbook: A Comprehensive Guide*. MathWorks, 3rd edition, 2023. ISBN 978-1-234-56789-0.
- [31] Paul Wilcox. BristolFE. <https://github.com/ndtatbristol/BristolFE>, 2024. Accessed: 14/04/2024.
- [32] Franz Aurenhammer and Rolf Klein. Voronoi diagrams. *Handbook of computational geometry*, 5(10): 201–290, 2000.
- [33] Qiang Du, Maria Emelianenko, and Lili Ju. Convergence of the lloyd algorithm for computing centroidal voronoi tessellations. *SIAM journal on numerical analysis*, 44(1):102–119, 2006.
- [34] James J Kuffner. Effective sampling and distance metrics for 3d rigid body path planning. In *IEEE International Conference on Robotics and Automation, 2004. Proceedings. ICRA'04. 2004*, volume 4, pages 3993–3998. IEEE, 2004.
- [35] Rasmus B Frandsen, Thomas Christiansen, and Marcel AJ Somers. Simultaneous surface engineering and bulk hardening of precipitation hardening stainless steel. *Surface and Coatings Technology*, 200(16-17): 5160–5169, 2006.
- [36] Thomas L Christiansen and Marcel AJ Somers. Low-temperature gaseous surface hardening of stainless steel: The current status. *International Journal of Materials Research*, 100(10):1361–1377, 2009.
- [37] SM Levcovici, DT Levcovici, V Munteanu, MM Paraschiv, and A Preda. Laser surface hardening of austenitic stainless steel. *Journal of materials engineering and performance*, 9(5):536–540, 2000.
- [38] Granta Design. *EduPack Software Package*. Granta Design, 2023. URL <https://www.grantadesign.com/products/edupack/>. Version 2023 R2, Accessed: 14/04/2024.
- [39] Scott R Eliason. *Maximum likelihood estimation: Logic and practice*. Number 96. Sage, 1993.